Supporting Information

Cohen et al. 10.1073/pnas.1418733111

SI Materials and Methods

SI Microdiffractometer

Core to the microdiffractometer design is an Aerotech ABR1000 air bearing used for the ϕ-rotation axis with rotation speeds of >360°/s. The sample is moved by a range of ±2.5 mm in the x and y directions by high-stiffness stages mounted on the air-bearing stage. A lift stage is used for vertical positioning of the ϕ axis to the X-ray interaction region and a linear stage provides horizontal motion by moving the entire lift stage and air-bearing assembly. The horizontal stage offers 10 mm of operational translation (within a sphere of confusion of 1.2 μm) and an overall length adjustment of 100 mm (upgradable to 400 mm) to accommodate long sample holders. During assembly and testing, careful measurement and adjustment of component orientation ensures that the air-bearing axis, horizontal stage, and sample lift stage motions are in close alignment. Rapid calibration of translations is achieved by home switches or precision absolute encoders. Table S1 lists the operational parameters of the microdiffractometer. The current horizontal positioning stage of the microdiffractometer translates sample holders at a maximum rate of 3 mm/s, enabling it to introduce a new crystal into the X-ray interaction region well before the readout time of the Rayonix MX325HE detector. To optimize thermal stability, the device is contained inside an insulating enclosure (Fig. S1). For measurements at cryogenic temperatures, an on-axis cryocooler nozzle geometry (Fig. 1 and Fig. S1) provides optimal temperature stability along the length of the sample mount. A heated shield just behind the sample holder magnet covers a small hole (20 mm) in the insulated enclosure that serves as a conduit for a zirconium support rod. The support rod, with minimal thermal conductivity, is used to connect the sample magnet and heating shield to the positioning stages.

Samples on the microdiffractometer are visualized with an in-line camera system (Fig. 1) with motorized zoom that consists of a 1” × 1.4”-diameter fixed elliptical mirror, with a 1.5-mm hole to pass X-rays, that reflects the sample image to a high-resolution camera assembly located below the X-ray path. Samples are illuminated by two sources: a backlight that is pneumatically inserted for imaging and withdrawn for data collection, and a stationary fiber optic side light (Fig. 1 B and C). A small-aperture X-ray scatter guard and beamstop assembly is pneumatically inserted into the beam path for data collection and removed to visualize the sample (Fig. 1 B and C), and is mounted on a motorized five-axis stage for alignment. The beamstop consists of a small-diameter stainless-steel cup, filled with a eutectic alloy of gallium, indium, and tin, and backed by a 5-mm–thick tungsten slug.

SI Single-Shot Spectrometer

The photon energy distribution for each X-ray pulse used to collect a diffraction pattern was recorded during the hydrogenase and myoglobin experiments using an energy spectrometer composed of a thin cylindrically bent silicon membrane that directs and disperses a small fraction of the X-ray pulse (<1% of the incident intensity) to a Ce:YAG screen (1). A 12-bit 120-Hz CCD camera with microscope optics was used to record the dispersed spectrograph. This method is one of the available options for characterizing the X-ray pulse energy at LCLS XPP (2–5). The spectrometer data were calibrated by cross-referencing its measured XFEL average spectrum with the scanning average measurement using a channel-cut monochromator. A typical spectrum obtained from a single X-ray pulse and typical averaged spectrum using measurements from 120 X-ray pulses is shown in Fig. S2. The single-pulse photon energies used for analyzing still diffraction images was determined by calculating the centroid of the calibrated energy spectrum.

SI Data Collection Strategy Calculation

To optimize completeness, the helical data collection mode includes an option to calculate a data collection strategy. A location on the end of the crystal is defined by the experimenter to collect a still diffraction pattern to use for the strategy calculation. The optimal starting orientation and predicted completeness are calculated using a script running MOSFLM (6) that is based on the WebIce (7) strategy option originally implemented for multicrystal data collection at SSRL BL12-2. A still diffraction pattern (or groups of patterns from oscillation data collection) is analyzed, and the best rotation range to use for data collection calculated, taking into consideration the beam size and the length of the crystal. A strategy interface within Blu-Ice enables data collected from previous crystals to be added to or excluded from the strategy calculation with the purpose to minimize the number of crystals required to obtain a complete dataset (Fig. S4). The resulting strategy is imported into the data collection interface by a push of a button from within the control software.

SI Sample Mounting Grid

Each grid is fabricated out of thin (100 μm) polycarbonate plastic, with multiple holes (or ports) that can hold either larger crystals in known locations or groups of smaller crystals. The prototype grid layout (Fig. S5) contains 75 ports: 15 ports of 125-μm diameter, 15 ports of 200-μm diameter, and 45 ports of 400-μm diameter. Custom grids with different hole shapes, sizes, and layouts may be easily fabricated and their layouts incorporated into the data collection software. The grid is compatible with most automated sample mounting robots and can reliably fit inside the port of a SSRL cassette and SAM robot grippers. Grids may be manually filled with crystals and flash frozen. Alternatively, a number of automated methods have been developed to load grids with crystallization solutions and specialized containers have been designed for growing crystals within grids using vapor diffusion techniques or with LCP within glass sandwich plates.

SI Grid Alignment

Data collection using grids starts with a semiautomated alignment procedure. After the grid is mounted onto the microdiffractometer, it is rotated edge-on in the in-line camera view, and the edge of the grid is clicked by the experimenter from within the software video display to move it into the X-ray interaction region (and center of rotation of the microdiffractometer). The grid is then rotated by 90°. The centers of four holes, two on each side of the grid, are next clicked in the video display to set the grid rotation and orientation (Fig. S6). From this information, the location of all of the grid holes is calculated and overlaid on the video view of the grid. This process may be completely automated using video analysis to orient the grid and identify the hole locations. Similar strategies may be carried out for other high-density sample containers of consistent dimensions.

SI Pol II–TFIIB–NAS

To study the conformational changes that take place during loading of a transcription bubble into the RNA polymerase active site, a full-length DNA scaffold 54 nt long with 25 noncomplementary base pairs (TB-25), constituting an artificial transcription bubble, was assembled into a complex with RNA polymerase II (Pol II)

and general transcription factor IIB (TFIIB). Pol II and TFIIB were purified as described previously (8). To assemble the Pol II–TFIIB–TB-25 complex, Pol II was first incubated with 2.5 M excess DNA/RNA scaffold in the presence of 1 mM $MgCl_2$. Size exclusion chromatography (SEC) was used to remove excess DNA/RNA scaffold from the sample. The eluted Pol II–TB-25 fraction was incubated with 2 M excess TFIIB in the presence of high salt (1.5 M NaCl) for 60 min followed by a second SEC step to remove excess TFIIB and lower the salt concentration to 100 mM NaCl. The presence of the TB-25 was corroborated using ethidium bromide staining. The complex was concentrated to 8 mg/mL for crystallization trials.

Early crystallization condition screening results were examined using a selection protocol combining bright-field microscopy, UV fluorescence microscopy, and dynamic light scattering to detect crystallization drops containing nanometer-sized crystals (NCs); and transmission electron microscopy (TEM) to accurately identify protein NCs and determine NC quality (9). A crystallization condition containing 32% (vol/vol) Tacsimate, 100 mM Hepes, pH 7.5, 10 mM DTT, and 2% (vol/vol) glycerol yielded high-quality NCs (0.5–3 μm in size) and was used to generate several milligrams of NC slurry of ∼30% (wt/vol). NCs were used with the GDVN injector for XFEL diffraction screening experiments at LCLS-CXI (10). Diffraction patterns were recorded at 120 Hz using 10-keV X-ray pulses of 40-fs duration with focus size of 200 nm at the X-ray interaction region and a Cornell-SLAC Pixel Array detector (11). The patterns were analyzed in real time with cctbx.xfel (12). Although the hit rate was low, a few patterns were observed with diffraction to 4.0 Å.

Efforts to produce larger crystals using a NC seeding technique (9) ultimately resulted in the production of larger crystals (of up to about 50 μm). Using this technique, a batch of crystals were grown inside grids using a specialized crystallization tray and flash frozen. During diffraction screening experiments, each grid was mounted on the goniometer using the SAM robot and the semiautomated grid alignment procedure described above was performed. Grid ports containing crystals were centered in the sample camera view. To collect still diffraction images, crystals were either identified by the experimenter through examination of the sample video display and centered into the X-ray interaction region, or a region of the port was selected for raster data collection.

Crystals were screened in this manner using the goniometer setup at LCLS-XPP with an X-ray beam size of 20 μm × 20 μm, energy of 9.6 keV, and 30-fs pulse length. Although there was only enough beam time available to screen a handful of crystals, a few of these were observed to diffract to 3.3-Å resolution. A larger number of crystals from the same crystallization batch were subsequently screened in grids at SSRL BL12-2 using a 20 μm × 20-μm or 10 μm × 10-μm beam size. The X-ray dose used to collect a single exposure from fresh crystals was incremented until improvements in resolution were no longer obtained, and observed resolution began to decrease (this corresponded to an optimal dose of about 35 MGy per frame). The best diffraction observed was only 3.7 Å. Diffraction quality screening results are summarized in Table S2. To determine the resolution limit, a peak search using the program ADXV (13) was used to locate diffraction peaks with I/σ of greater than 2. Those at the outer edge of the pattern were then visually examined at multiple locations at high zoom, noting the counts in the peak pixels relative to the background pixels and verifying that the peak fits the crystal lattice. The resolution shell that gave a reasonable number of acceptable peaks was then specified as the maximum resolution for that image.

SI β_2-Adrenoreceptor

Crystals of β_2-adrenoreceptor bound the agonist BI167107 and a nanobody that stabilizes the active state (Nb6B9) were obtained as described previously (14). Crystals ranging in size from 20 to 100 μm were mounted on MiTeGen micromeshes (www.mitegen.com/) and screened at LCLS for diffraction quality by collecting still diffraction patterns using an X-ray beam size of 3 μm × 3 μm or 50 μm × 50 μm and energy of 9.0 keV. Crystals were either identified by the experimenter through examination of the sample video display and centered into the X-ray interaction region, or a region of the port was selected for raster data collection. The crystals used were from the same crystallization batch as those used for the initial structure determination at a synchrotron (14), allowing for direct comparison of their diffraction from these different X-ray sources.

SI CpI

CpI [FeFe]-hydrogenase from *Clostridium pasteurianum* was purified with slight modifications to the previously described methods (15). Q-Sepharose Fast Flow resin was substituted for DEAE resin, and Sephacryl S-200 resin was substituted for Sephadex G-100 resin; the hydroxyapatite step was excluded. Crystals were grown using the microcapillary batch diffusion method with a precipitating solution containing 25% (wt/vol) PEG 4000, 0.1 M sodium acetate, 0.2 M ammonium sulfate, and 1 mM sodium dithionite to remove trace oxygen (16). A protein solution containing 30 mg/mL protein, 50 mM Tris (pH 8.0), 0.2 M KCl, and 1 mM sodium dithionite was allowed to gradually equilibrate with the precipitating solution, and large brown crystals (>400 μm) were observed in approximately 2 wk. All sample manipulations were carried out under anaerobic conditions in an MBraun Unilab glove box with 100% nitrogen atmosphere. Before data collection, CpI crystals were cryoprotected by equilibrating them in crystallization solution supplemented with 14% (vol/vol) glycerol in the presence of 1 mM sodium dithionate and then subsequently flash cooled in liquid nitrogen on large nylon loops (0.8–1.0 mm).

Data collection was performed using the helical data collection mode, with an unattenuated 50-μm beam size and a photon energy of 9,017 eV. Five crystals, with lengths ranging from 1 to 3 mm, were used for data collection. Crystals were translated by 70 μm and rotated by 0.5° between exposures, and a total of 162 images were collected. Eleven degrees of oscillation data were collected at the first position exposed on the crystal. Still data were processed using both IPMOSFLM/SCALA and cctbx-xfel and data processing statistics are given in Table S3. The available version of the program XDS (17) could not be used to process still diffraction patterns, but was used to analyze the oscillation images corresponding to each crystal. In some cases, for example when the crystal was very mosaic or split at the first position exposed, IPMOSFLM was instead used to index and postrefine a group of still images from the same crystal.

For the IPMOSFLM (6) protocol, postrefined orientation and experimental parameters obtained from the oscillation data were used as input for integration of the still diffraction patterns using a fake oscillation angle of 0.02°. The crystals were processed individually and visual examination of images that had large scale factors confirmed that the corresponding areas of the crystals were of poor diffraction quality. These images were manually rejected before scaling and merging, producing a final dataset comprising 110 images. For cctbx-xfel processing, all 162 images were used, and 4 were rejected by the program. To check the quality of the data, both datasets were scaled to a synchrotron dataset collected from a single Cpl crystal from the same crystallization experiment. The CCP4 program SCALEIT (18) was used to compare the datasets giving a R factor of 30% and a weighted R factor of 13%. Although it was found that the datasets were essentially isomorphous with the synchrotron data, there were some differences that could possibly be attributed to the presence of radiation damage in the case of the synchrotron dataset, compared with the essentially damage-free femtosecond dataset in the case of the LCLS data.

The Cpl structure was solved by molecular replacement (MR) using the program MOLREP with both the MOSFLM/SCALA

and cctbx-xfel datasets. The starting model for MR was the *C. pasteurianum* [FeFe]-hydrogenase (PDB ID code 3C8Y) with the Fe-S clusters and associated ligands removed. The MR solution was refined for 15 cycles of XYZ and B refinement using the program REFMAC (19). MR and refinement statistics are listed in Table S3. The $2F_o - F_c$ and $F_o - F_c$ electron density maps calculated following refinement showed the location of the Fe-S clusters and the Fe-Fe prosthetic groups (Fig. 5 *A* and *B*). Peak heights for the iron atoms were between 10 and 11 σ, and the peak heights for the sulfur atoms in the Fe-S cluster were between 4.5 and 5.5 σ. To check the quality of the data and the subsequent electron density maps, several contiguous regions of the Cpl polypeptide chain, amounting to about 5% each time, were removed and the truncated model submitted to simulated annealing refinement using PHENIX, and omit electron density omit calculated. These maps, contoured at 1.0 σ, showed the presence of the omitted sections of polypeptide.

SI Myoglobin

Crystallization of recombinant sperm whale myoglobin in the space group *P*6 was performed as previously described (20), with the following modifications: the drop was allowed to equilibrate for 1 d; 1,000-fold–diluted solution was used to seed crystals; and the well solution did not include EDTA. Myoglobin crystals were harvested from hanging drops. The grid was covered with a thin coat of Paratone-N (Parabar 10312; Hampton Research). Individual crystals were picked out of the drop using a nylon loop tool, placed inside a drop of Paratone-N, and then placed inside a grid port. The size of the crystal and the size of the grid port were matched as closely as possible.

Data were collected using a 50-μm focus at a nominal energy of 9.5 keV from crystals within 32 grids with the following protocol: (*i*) the port containing the crystal was centered and single X-ray pulse was used to collect a still diffraction pattern. (*ii*) Eleven degrees of oscillation data were collected around the still image location using multiple attenuated pulses (Fig. S7). (*iii*) A second still diffraction pattern was collected. The energy spectrum was measured for each pulse used for data collection, although thus far only the mean pulse energy has been used for data processing. Data from a total of 932 crystals were collected.

Because *P*6 is a polar space group, the diffraction pattern can be indexed in two nonequivalent indexing schemes, with the sixfold rotation axis pointing in a positive or negative direction. Attempts to merge data from different crystals arbitrarily indexed will result in apparent merohedral twinning with the twinning operation k,h,–l. Although the Brehm and Diederichs algorithm (21) has been developed to solve the indexing ambiguity for data consisting of single still diffraction patterns from multiple crystals, it was not available at the time of the experiment. However, using the oscillation data (Fig. S7) that were collected around the position of each still pattern collected, it was quite straightforward to determine the indexing relationship between each of the crystals and that of an arbitrarily chosen reference by comparing the intensities of the reflections related by the above-mentioned operation with the program POINTLESS (22). The oscillation data could be processed like conventional oscillation data, using the program XDS (17) for autoindexing, integration, and postrefinement, and the CCP4 program SCALA (22) for scaling and merging the data from each crystal. A total of 637 crystals could be indexed in the correct space group and unit cell following this procedure.

These oscillation data were also used to produce an isomorphous "reference dataset" used for scaling and to solve the indexing ambiguity of the still diffraction images processed using the program cctbt.xfel (following the second protocol described below). This reference dataset was obtained by scaling and merging the 11° oscillation data from 100 arbitrarily chosen crystals (Table S4).

Two different data processing protocols were carried out to process the still diffraction patterns, and the results are compared in Table S2. For the first approach, the postrefined orientation and experimental parameters obtained from the oscillation data of 637 crystals (determined as described above) were used as input for integration of the still diffraction patterns with the program IPMOSFLM (6) using a fake oscillation angle parameter of 0.05°. The integrated reflections for each crystal were scaled and merged with SCALA. Although this approach used a flawed partiality estimate and resulted in the rejection of many diffraction images because of large differences in scale between the reflection intensities, the data from 253 still shots yielded a dataset 98.8% complete to 1.48 Å that showed no evidence of twinning. Molecular replacement phasing was carried out using the PDB entry 1VXA as a model and the electron density map was inspected. To test that the recovery of features in the map was not due merely to bias, automated structure tracing from partial models using ARPwARP (23) was attempted; it was possible to trace the entire protein chain after omitting 57 residues (37%) of the model. The initial model could be refined to *R* factor of 28% (Table S4).

The second processing approach used the program cctbx.xfel (12), which was developed specifically to handle single still diffraction patterns acquired at XFELs. The reference dataset, produced using the oscillation data as described above, was used as isomorphous reference data for scaling and to solve the indexing ambiguity. The individual single-pulse still diffraction patterns were indexed imposing the known symmetry and the reflections integrated. The merged intensity values in the reference set were next used to scale and, when necessary, reindex the reflections from the still diffraction pattern on a per-image basis. The reference dataset was also used to reject data from images indexed in the wrong lattice. With this approach, more images could be included, and a better quality dataset to 1.36 Å was obtained that allowed tracing the structure omitting 62% of the chain and refining the structure to an *R* factor of 15.9% (Table S4).

SI Multiplexing

Multiplexing is achieved at the LCLS using two methods: a beam splitting mode that enables more than one experiment to operate simultaneously and a beam switching mode where a grazing incidence mirror is used to switch the entire beam between experiments for short periods (24). Beam splitting is achieved by passing the X-ray beam through a thin diamond crystal that selects out a monochromatic energy delivered to a first experiment while a large fraction of the incident beam is transmitted through the crystal for use by a second experimental setup (25).

1. Zhu D, et al. (2012) A single-shot transmissive spectrometer for hard x-ray free electron lasers. *Appl Phys Lett* 101(3):034103.
2. Chalupsky J, et al. (2011) Comparing different approaches to characterization of focused X-ray laser beams. *Nucl Instrum Methods Phys Res A* 631(1):130–133.
3. Dusterer S, et al. (2011) Femtosecond x-ray pulse length characterization at the Linac Coherent Light Source free-electron laser. *New J Phys* 13(2011):093024.
4. Ding Y, et al. (2012) Femtosecond x-ray pulse characterization in free-electron lasers using a cross-correlation technique. *Phys Rev Lett* 109(25):254802.
5. Loos H, Tschentscher T, Tiedtke K (2013) LCLS accelerator operation and measurement of electron beam parameters relevant for the x-ray beam. *Advances in X-Ray Free-Electron Lasers II: Instrumentation* (SPIE, Bellingham, WA), Vol 8778.
6. Leslie AGW, Powell HR, Read RJ, Sussman JL (2007) Processing diffraction data with MOSFLM. *Evolving Methods for Macromolecular Crystallography*, eds Read RJ, Sussman JL (Springer, New York), Vol 245, pp 41–51.
7. González A, et al. (2008) Web-Ice: Integrated data collection and analysis for macromolecular crystallography. *J Appl Cryst* 41(1):176–184.
8. Pullara F, et al. (2013) A general path for large-scale solubilization of cellular proteins: From membrane receptors to multiprotein complexes. *Protein Expr Purif* 87(2):111–119.
9. Stevenson HP, et al. (2014) Use of transmission electron microscopy to identify nanocrystals of challenging protein targets. *Proc Natl Acad Sci USA* 111(23):8470–8475.
10. Boutet S, Williams GJ (2010) The Coherent X-ray Imaging (CXI) instrument at the Linac Coherent Light Source (LCLS). *New J Phys* 12:035024.

11. Hart P, et al. (2012) The CSPAD megapixel x-ray camera at LCLS. X-ray free-electron lasers: Beam diagnostics, beamline instrumentation, and applications. *Proc SPIE* 8504: 85040C.
12. Hattne J, et al. (2014) Accurate macromolecular structures using minimal measurements from X-ray free-electron lasers. *Nat Methods* 11(5):545–548.
13. ADXV (2013) ADXV—a program to display X-ray diffraction images. Available at www.scripps.edu/~arvai/adxv.html. Accessed August 1, 2014.
14. Ring AM, et al. (2013) Adrenaline-activated structure of β2-adrenoceptor stabilized by an engineered nanobody. *Nature* 502(7472):575–579.
15. Chen JS, Mortenson LE (1974) Purification and properties of hydrogenase from *Clostridium pasteurianum* W5. *Biochim Biophys Acta* 371(2):283–298.
16. Peters JW, Lanzilotta WN, Lemon BJ, Seefeldt LC (1998) X-ray crystal structure of the Fe-only hydrogenase (CpI) from *Clostridium pasteurianum* to 1.8 angstrom resolution. *Science* 282(5395):1853–1858.
17. Kabsch W (2010) XDS. *Acta Crystallogr D Biol Crystallogr* 66(Pt 2):125–132.
18. Winn MD, et al. (2011) Overview of the CCP4 suite and current developments. *Acta Crystallogr D Biol Crystallogr* 67(Pt 4):235–242.
19. Murshudov GN, et al. (2011) REFMAC5 for the refinement of macromolecular crystal structures. *Acta Crystallogr D Biol Crystallogr* 67(Pt 4):355–367.
20. Cohen A, Ellis P, Kresge N, Soltis SM (2001) MAD phasing with krypton. *Acta Crystallogr D Biol Crystallogr* 57(Pt 2):233–238.
21. Brehm W, Diederichs K (2014) Breaking the indexing ambiguity in serial crystallography. *Acta Crystallogr D Biol Crystallogr* 70(Pt 1):101–109.
22. Evans P (2006) Scaling and assessment of data quality. *Acta Crystallogr D Biol Crystallogr* 62(Pt 1):72–82.
23. Langer G, Cohen SX, Lamzin VS, Perrakis A (2008) Automated macromolecular model building for X-ray crystallography using ARP/wARP version 7. *Nat Protoc* 3(7):1171–1179.
24. Yin J, et al. (2013) LCLS mirror switching of x-ray beam. *Proc SPIE* 8849:88490Q.
25. Zhu D, et al. (2014) Performance of a beam-multiplexing diamond crystal monochromator at the Linac Coherent Light Source. *Rev Sci Instrum* 85(6):063106.

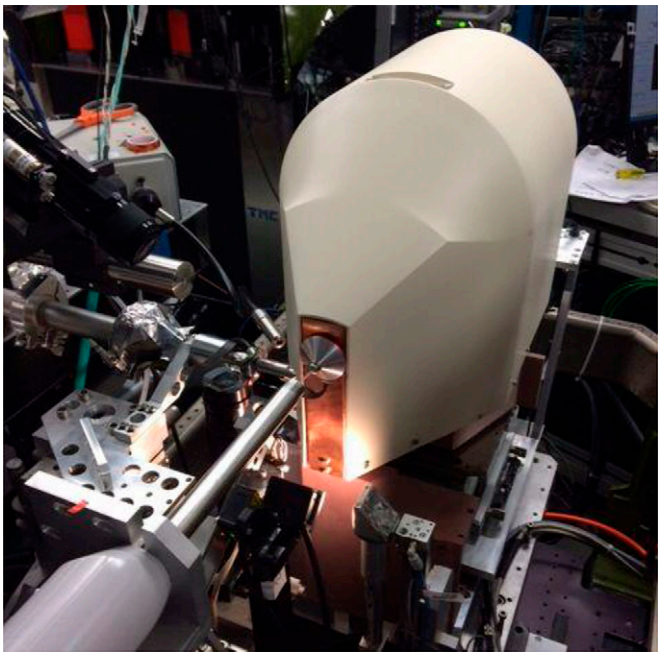

Fig. S1. Photograph of the diffractometer-based instrumentation installed at LCLS-XPP.

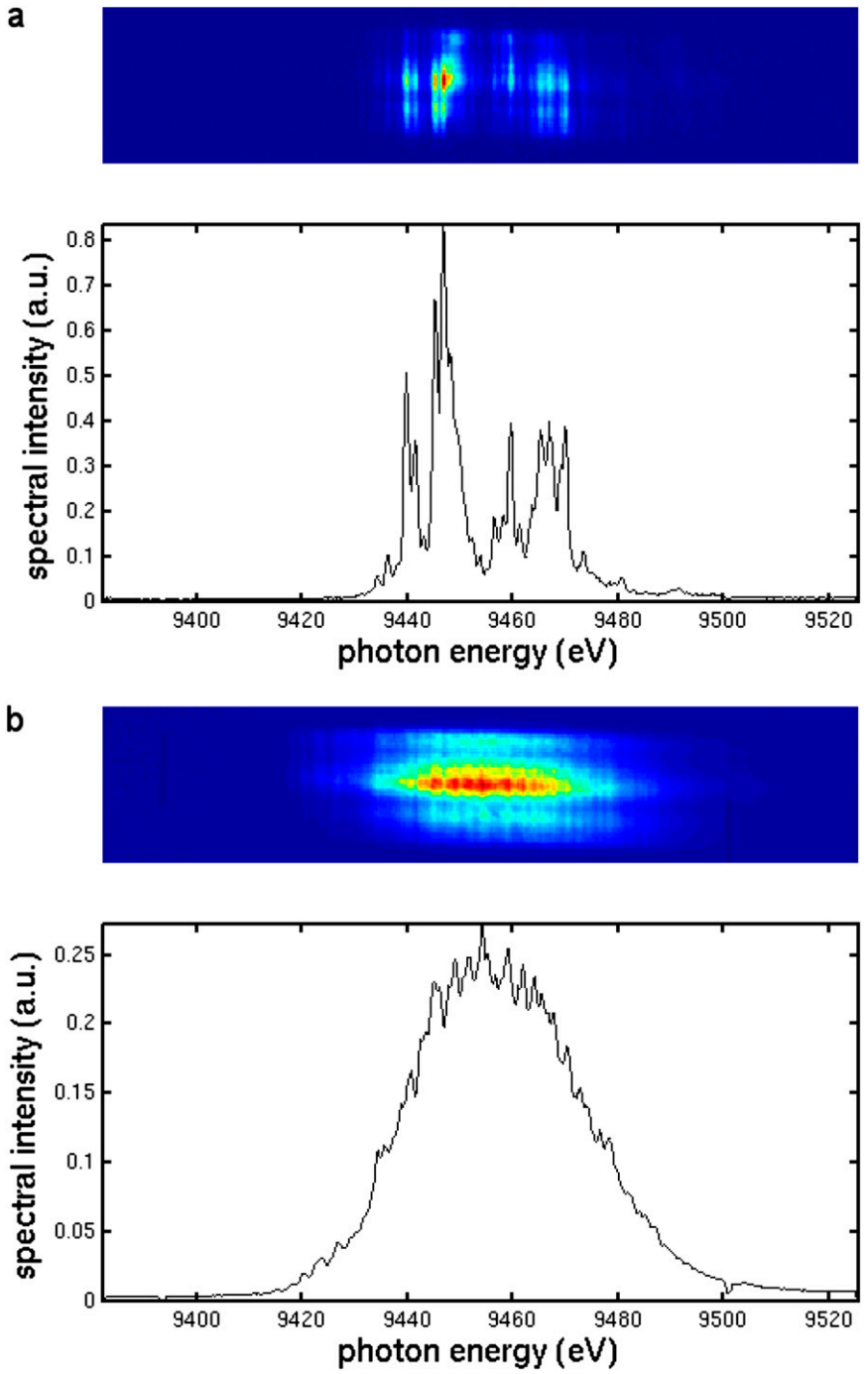

Fig. S2. Heat map of detector information and 2D graph of example spectrometer data. (*A*) Measured spectrum of a single LCLS self-amplified spontaneous emission pulse. (*B*) The average spectrum of 120 X-ray pulses for the collection of a single degree of oscillation data.

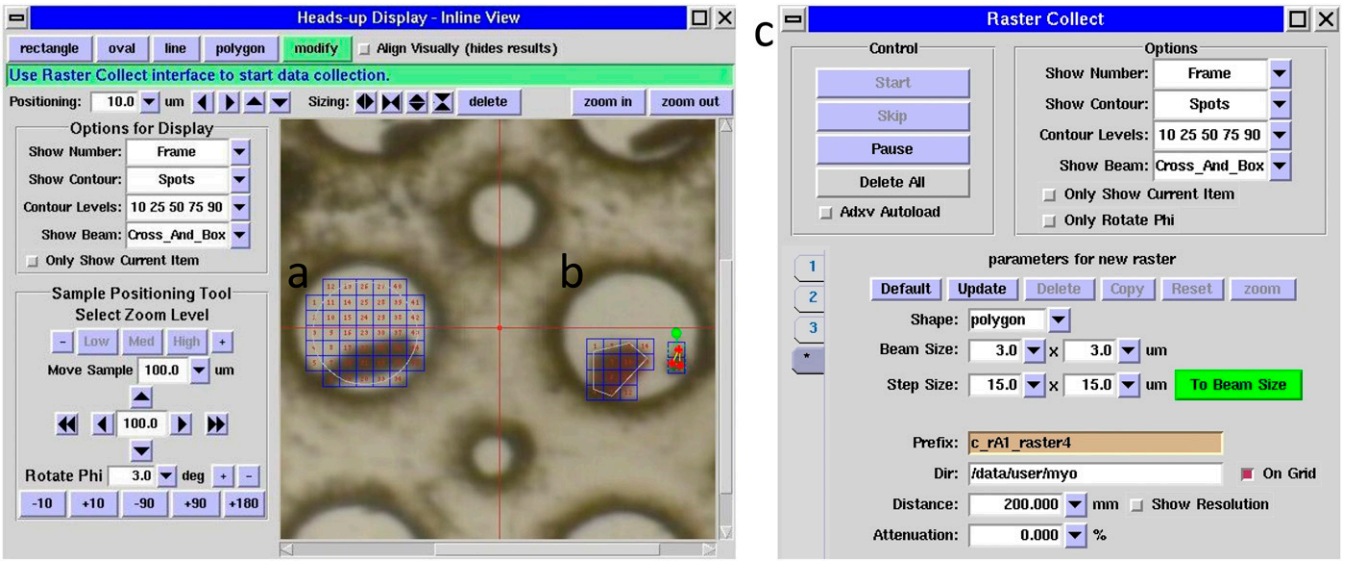

Fig. S3. Screen capture images of the Blu-Ice GUI illustrating the raster interface for specifying the area of the sample use for data collection. (*A*) Rastering the entire circular area of a grid hole. (*B*) Specific areas of the hole are selected for data collection. (*C*) Interface for specifying collection parameters.

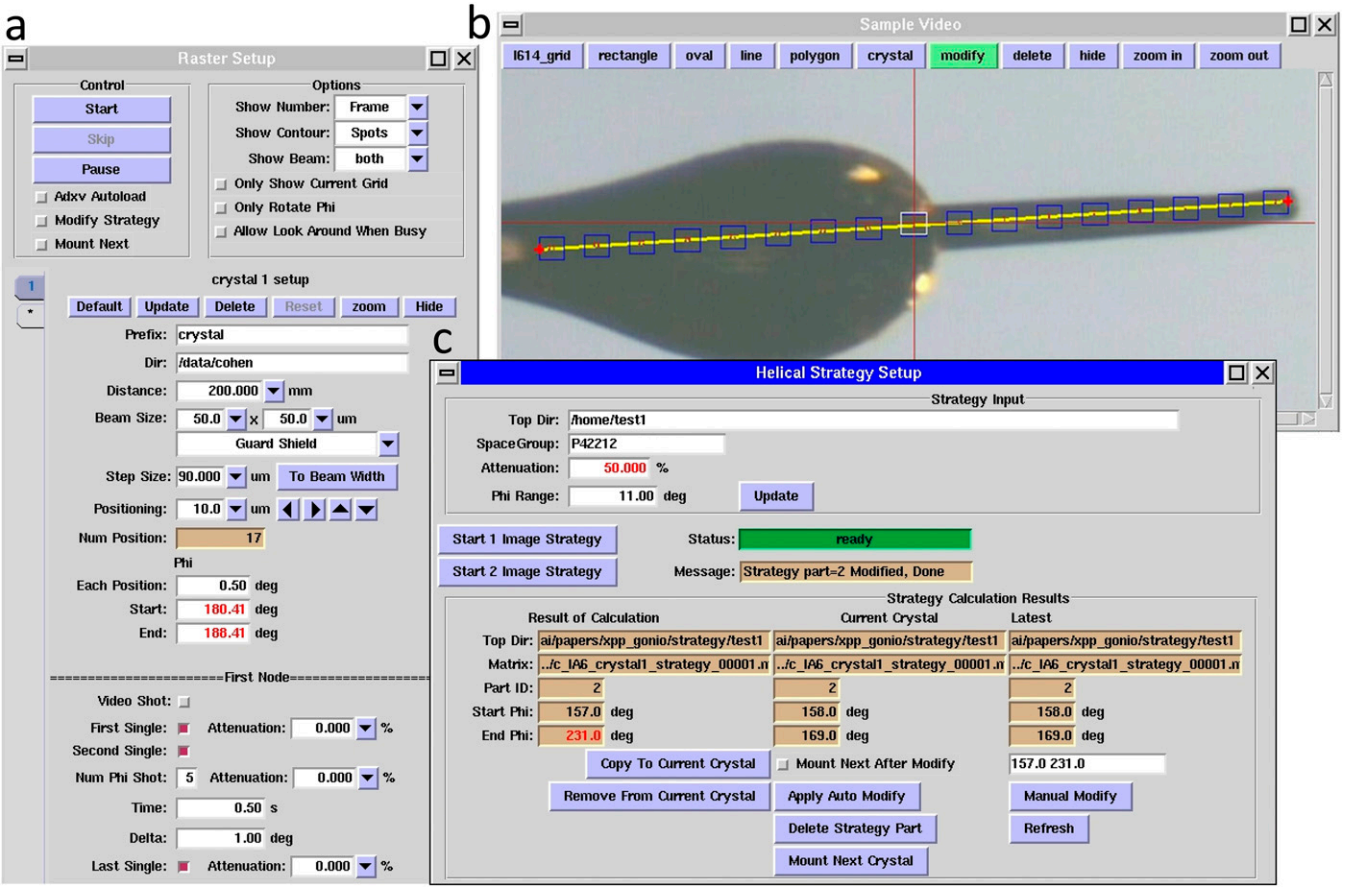

Fig. S4. Screen capture images of the Blu-Ice GUI illustrating the helical data collection mode. (*A*) Interface for specifying collection parameters; (*B*) video display of a Cpl crystal. The yellow line defines the crystal length and the overlaid boxes depict the locations for future exposure to a single X-ray pulse. (*C*) Interface for multicrystal data collection strategy determination.

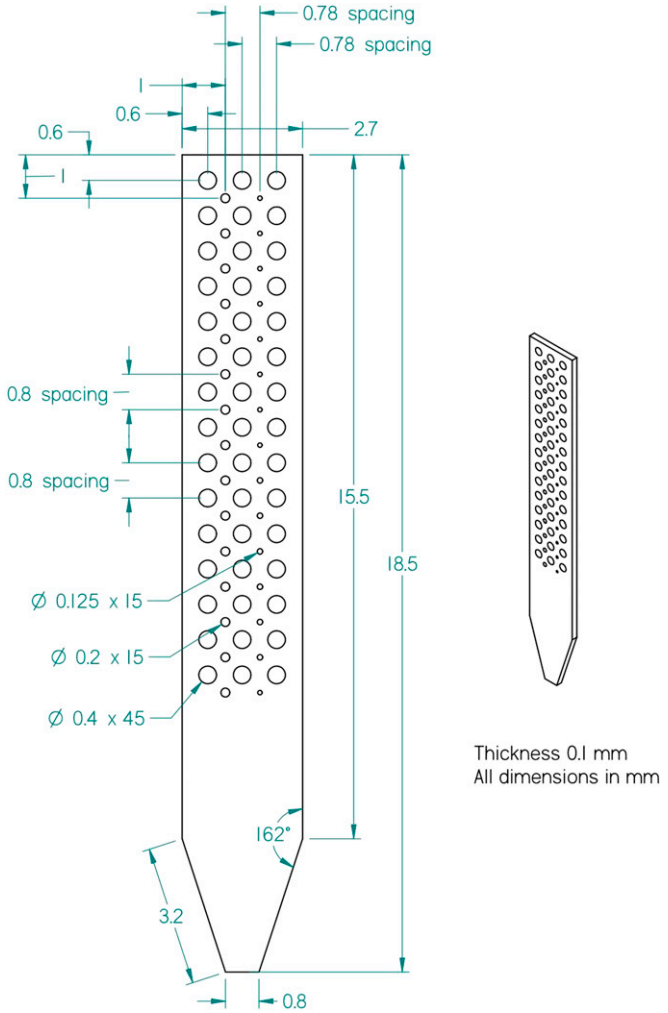

Fig. S5. Schematic of the polycarbonate high-density sample mounting grid.

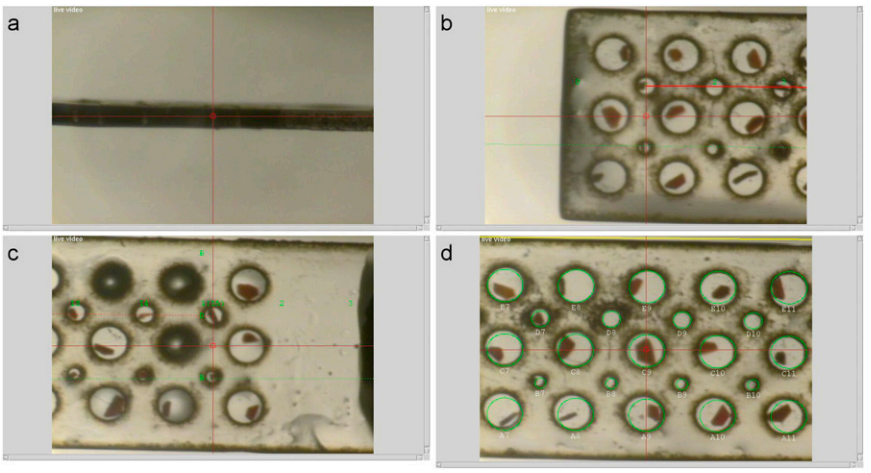

Fig. S6. Screen capture images of the Blu-Ice GUI illustrating the semiautomated grid alignment process. (*A*) The grid is aligned to be edge-on to the in-line camera view and the edge of the grid is moved into the X-ray beam position. (*B*) Two specific holes on one side of the grid are selected by clicking on their location inside the video display. (*C*) The grid is translated and the location of two holes on the opposite side of the grid are clicked next. *D* shows the completed calibration of the grid orientation in relation to the diffractometer axes and X-ray beam position.

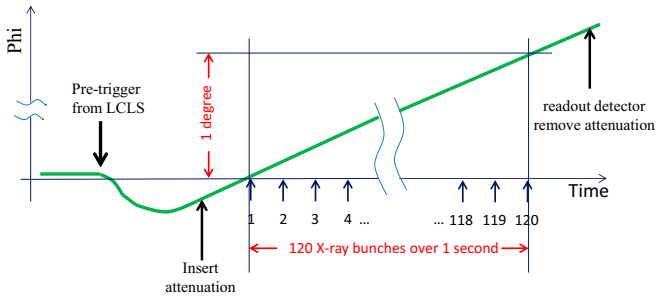

Fig. S7. Depiction of the events during oscillation data collection at LCLS-XPP. The green line illustrates the velocity of the ϕ-rotation axis that is rotated by 1°/s while the crystal is exposed to attenuated X-ray pulses at 120 Hz. The ϕ-angle versus bunch coincidence is better than 0.01°.

Table S1. The motion performance of the microdiffractometer

Axis	Range	Speed	Encoder/homing resolution	Motion increment
ϕ	Infinite	90°/s	0.1 milli-degrees	0.1 milli-degrees
Sample-*x*	2.5 mm	0.25 mm/s	0.1 μm	0.06 μm
Sample-*y*	2.5 mm	0.25 mm/s	0.1 μm	0.06 μm
Sample-horz	100 mm	3 mm/s	0.2 μm	0.09 μm
ϕ-vertical	13 mm	0.05 mm/s	0.2 μm	0.09 μm

Table S2. Comparison of diffraction quality screening results for Pol II–TFIIB–NAS

Largest crystal dimension, μm	Location	Delivery method	Best resolution observed, Å
5	LCLS-CXI	GDVN injector at RT	4.0
<50	SSRL BL12-2	Grids at 100 K	3.7
<50	LCLS-XPP	Grids at 100 K	3.3

Table S3. *Clostridium pasteurianum* hydrogenase data processing

Processing software	IPMOSFLM/SCALA	cctbx-xfel
Data collection/processing		
Cell dimensions, Å*	$a = b = 111.28$, $c = 103.81$	$a = b = 110.08$, $c = 103.01$
Resolution limits, Å	38.0–1.60	44.7–1.60
No. of images	110	158
Completeness, %	93.9 (88.0)	91.7 (62.4)
CC1/2[†]	0.48 (0.09)	0.39 (0.23)
Reflections, observed/unique	408,563/80,047	663,856/76,845
Molecular replacement and refinement[‡]		
RF/σ[§], background	9.9 (4.0)	11.4 (3.1)
Weighted *R* factor, %	42.8	42.2
Score[¶]	0.50	0.51
R_{work}, %	39.2 (34.6)	39.9 (35.8)
R_{free}, %	38.1 (38.9)	40.2 (38.7)
FOM[#]	0.63	0.55

The values in parentheses refer to the high-resolution shell (1.62–1.60 Å).
*Space group $P4_22_12$.
[†]The correlation coefficient between half datasets is defined in ref. 1.
[‡]Using MOLREP for molecular replacement and REFMAC for 15 cycles of refinement.
[§]Rotation function peak height from MOLREP.
[¶]The score is the product of the Correlation Coefficient of intensities and the maximal value of the Packing Function.
[#]The FOM is the overall figure of merit of the phases.

1. Karplus PA, Diederichs K (2012) Linking crystallographic model and data quality. *Science* 336:1030–1033.

Table S4. Myoglobin data processing

	Single-pulse data		Multiple-pulses oscillations
Processing software	IPMOSFLM/SCALA	cctbx-xfel	XDS/AIMLESS
Data collection/processing			
Resolution limits, Å	39.15–1.40	39.15–1.36	39.15–1.39
No. of images	253	739	1,100
Completeness, %	91.6 (45.7)	91.6 (31.0)	100 (99.7)
CC1/2*	0.767 (0.30)	0.956 (0.752)	0.955 (0.07)
Reflections, observed/unique	560,156/37,257	1,299,845/43,737	1,797,835/43,459
Molecular replacement and refinement[†]			
RF/σ[‡], background	7.26	8.58	—
Weighted *R* factor, %	55.9	48.4	—
Score[§]	0.577	0.664	—
R_{work}, %	28.5 (45.0)	15.9 (38.5)	16.4 (28.8)
R_{free}, %	31.5 (46.0)	18.8 (38.9)	17.9 (32.7)

The values in parentheses correspond to the highest resolution bin.
*The correlation coefficient between half datasets is defined in ref. 1.
[†]Using MOLREP for molecular replacement and Phenix for refinement.
[‡]Rotation function peak height from MOLREP.
[§]The score is the product of the Correlation Coefficient of intensities and the maximal value of the Packing Function.

1. Karplus PA, Diederichs K (2012) Linking crystallographic model and data quality. *Science* 336:1030–1033.